Electric Field-Controlled Interfacial Polarization Coupling in van der Waals Ferroelectric Heterojunctions

Wei Li(李伟)[1,2,3], HengLiu(柳衡)[1,2,3], and Hualing Zeng(曾华凌)[1,2,3*]

[1]*International Center for Quantum Design of Functional Materials, Hefei National Research Center for Physical Sciences at the Microscale, University of Science and Technology of China, Hefei 230026, China*
[2]*Key Laboratory of Strongly Coupled Quantum Matter Physics, Department of Physics, Chinese Academy of Sciences, University of Science and Technology of China, Hefei 230026, China*
[3]*Hefei National Laboratory, University of Science and Technology of China, Hefei 230088, China*

(Received 22 December 2024; accepted manuscript online 31 March 2025)

Recent advances in van der Waals (vdW) ferroelectrics have sparked the development of related heterostructures with non-volatile and field-tunable functionalities. In vdW ferroelectric heterojunctions, the interfacial electrical characteristics play a crucial role in determining their performance and functionality. In this study, we explore the interfacial polarization coupling in two-dimensional (2D) ferroelectric heterojunctions by fabricating a graphene/h-BN/$CuInP_2S_6$/α-In_2Se_3/Au ferroelectric field-effect transistor. By varying the gate electric field, the $CuInP_2S_6$/α-In_2Se_3 heterojunction displays distinct interfacial polarization coupling states, resulting in significantly different electrical transport behaviors. Under strong gate electric fields, the migration of Cu ions further enhances the interfacial polarization effect, enabling continuous tuning of both the polarization state and carrier concentration in α-In_2Se_3. Our findings offer valuable insights for the development of novel multifunctional devices based on 2D ferroelectric materials.

DOI: 10.1088/0256-307X/42/5/057501 CSTR: 32039.14.0256-307X.42.5.057501

The interfacial polarization coupling in ferroelectric heterojunctions significantly influences the charge redistribution, band structure, carrier transport characteristics, and the ferroelectric properties of the interfacial region.[1–4] However, studying the interfacial effects of polarization coupling in conventional ferroelectric oxides presents several challenges, including lattice mismatch and surface reconstruction issues.[5,6] Overcoming these challenges requires the construction of ideal ferroelectric heterojunctions. 2D materials, with their clean and dangling-bond-free surfaces, provide an ideal platform for exploring the mechanisms of ferroelectric interfacial polarization coupling. In recent years, 2D layered ferroelectric materials and their heterostructures have garnered significant attention due to their potential for fabricating a variety of functional devices with atomic thickness. Room-temperature 2D ferroelectric materials, such as $CuInP_2S_6$,[7–13] α-In_2Se_3,[14–17] and SnS,[18,19] exhibit stable electric polarizations even at thicknesses of a few atomic layers. This remarkable stability makes them promising candidates for constructing non-volatile memory and neuromorphic devices and systems.[20] The development of ultrathin vdW ferroelectric heterojunctions effectively addresses traditional interface challenges and offers a unique opportunity to explore the influence of ferroelectric interfacial polarization coupling on electrical transport properties.

Recent studies have shown that $CuInP_2S_6$, as a ferroelectric insulator, exhibits a relatively large coercive field, while α-In_2Se_3, as a ferroelectric semiconductor, displays a comparatively smaller coercive field. Both materials belong to the van der Waals (vdW) system, which facilitates the construction of 2D ferroelectric heterojunctions. For example, Sung *et al.*[21] reported a fully ferroelectric field-effect transistor (FeFET) based on a $CuInP_2S_6$/h-BN/α-In_2Se_3 heterojunction. At low electric fields, the enhanced ferroelectric polarization coupling at the $CuInP_2S_6$/h-BN/α-In_2Se_3 interface significantly improved the memory performance of the device. However, due to the electrochemical activity of $CuInP_2S_6$,[22] Cu ion migration under high electric fields may lead to more complex polarization coupling effects at the $CuInP_2S_6$/α-In_2Se_3 interface, which is still under exploration.

In this work, we investigate interfacial polarization coupling in 2D ferroelectric heterojunctions by using FeFET of graphene/h-BN/$CuInP_2S_6$/α-In_2Se_3/Au. Specifically, we systematically examine how different interfacial polarization coupling states influence electrical transport characteristics. When the gate electric field is within the coercive fields of α-In_2Se_3 and $CuInP_2S_6$, the transport behavior of α-In_2Se_3 is primarily determined by its intrinsic ferroelectric semiconductor properties. When the gate voltage exceeds the coercive field of $CuInP_2S_6$ but remains below its threshold field, the polarization directions of $CuInP_2S_6$ and α-In_2Se_3 align. The polarization of $CuInP_2S_6$ reduces the coercive field of α-In_2Se_3, resulting in a significant change in its transport behavior. Once the gate electric field surpasses the threshold field

*Corresponding author. Email: hlzeng@ustc.edu.cn
© 2025 Chinese Physical Society and IOP Publishing Ltd. All rights, including for text and data mining, AI training, and similar technologies, are reserved.

of $CuInP_2S_6$, Cu ions migrate to the interface, forming a strong interfacial electric field that further modulates the coercive field and transport behavior of α-In_2Se_3. Additionally, temperature-dependent experiments confirm the critical role of Cu ion migration in modulating the ferroelectric polarization and carrier concentration in α-In_2Se_3. Our results provide valuable insights for the future development of multifunctional devices based on 2D vdW ferroelectric materials.

Figure 1(a) shows the schematic of crystal structure of $CuInP_2S_6$ and α-In_2Se_3. Both $CuInP_2S_6$ and α-In_2Se_3 exhibit out-of-plane ferroelectric polarization at room temperature. The ideal P–E curves for $CuInP_2S_6$ (in red) and α-In_2Se_3 (in black) are displayed in Fig. 1(b), which demonstrate counterclockwise hysteresis loops. The coercive fields of α-In_2Se_3 and $CuInP_2S_6$ are denoted as E_{Cr1} and E_{Cr2}, respectively, with E_{th} representing the threshold field for Cu ion migration in $CuInP_2S_6$. It has been shown that E_{Cr2} is relatively larger than E_{Cr1}.[21] Therefore, in ferroelectric heterojunction of $CuInP_2S_6/\alpha$-In_2Se_3, complex polarization coupling effect and external field control are expected. Here, we define the applied external field (E) as E_1 and E_2 with $E_{Cr1} < E_1 < E_{Cr2}$ and $E_{Cr2} < E_2 < E_{th}$.

Figure 1(c) depicts the different interfacial polarization states of $CuInP_2S_6/\alpha$-In_2Se_3 under a low electric field $|E_1|$, where the polarization direction of $CuInP_2S_6$ remains unchanged, and the polarization direction of α-In_2Se_3 aligns with the electric field E_1. Owing to the interfacial pinning effect at the $CuInP_2S_6/\alpha$-In_2Se_3 interface, the P–E curve of α-In_2Se_3 exhibits a shifted ferroelectric hysteresis, as shown in Fig. 1(d). The purple and blue solid lines indicate the shifted P–E curves of α-In_2Se_3 with $CuInP_2S_6$ polarized upward and downward, respectively. It is noteworthy that the P–E curve shown in Fig. 1(d) represents the ferroelectric properties of α-In_2Se_3 modulated by $CuInP_2S_6$, rather than the overall performance of the $CuInP_2S_6/\alpha$-In_2Se_3 heterostructure (the P–E hysteresis loops of the $CuInP_2S_6/\alpha$-In_2Se_3 heterostructure are presented in Fig. S1 in Supplementary Material). In contrast, when an external electric field of $|E_2|$ is applied, the polarization directions of $CuInP_2S_6$ and α-In_2Se_3 eventually align, as shown in Fig. 1(e). It is the P–E curve of α-In_2Se_3 that should follow only half routes of the shifted ferroelectric hysteresis by switching the field from $+E_2$ to $-E_2$ and back, with the left side in the case of $CuInP_2S_6$ polarized upward (purple) and the right side in the case of $CuInP_2S_6$ polarized downward (blue) in Fig. 1(d). As a result, across the complete cycle, the P–E curve of α-In_2Se_3 narrows as represented by the black solid line in Fig. 1(f). The window size of the ferroelectric hysteresis can be determined by the polarization strength of $CuInP_2S_6$. Additionally, when $|E| > E_{th}$, the Cu ions in $CuInP_2S_6$ migrate across layers along the gate field direction, further enhancing the polarization strength of $CuInP_2S_6$. This effect further increases the interfacial effects of polarization coupling, potentially narrowing or even reversing the P–E curve window of α-In_2Se_3.

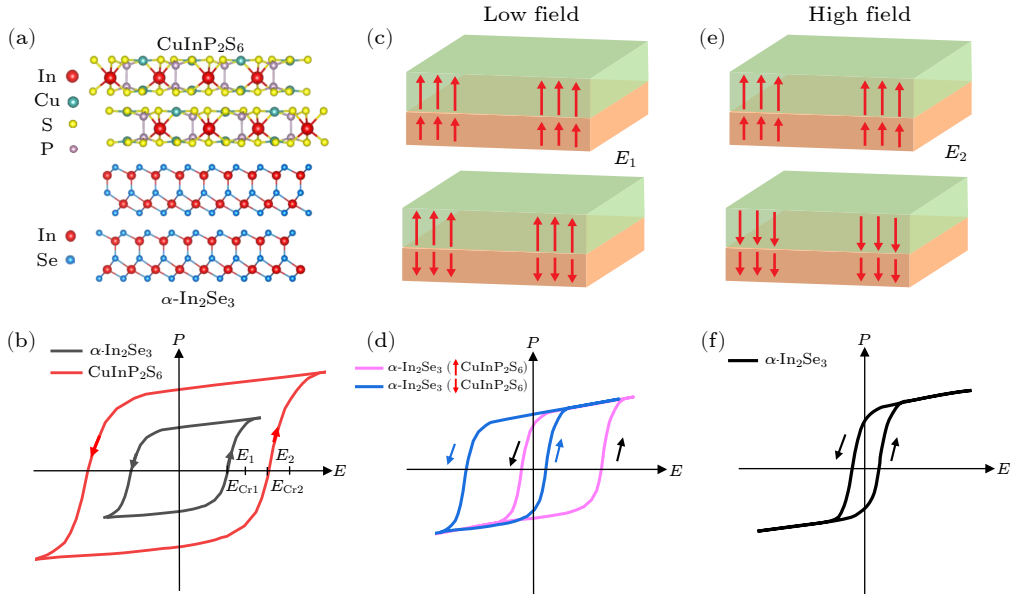

Fig. 1. Crystal structure and the P–E curve of α-In_2Se_3 in the $CuInP_2S_6/\alpha$-In_2Se_3 heterostructure under varying electric fields. (a) Schematic of the crystal structure of the $CuInP_2S_6$ and α-In_2Se_3. (b) Ideal P–E curves for $CuInP_2S_6$ (red solid line) and α-In_2Se_3 (black solid line), where E_1 is below the coercive field of $CuInP_2S_6$ (E_{Cr2}), and E_2 is above E_{Cr2}. (c) Polarization of the $CuInP_2S_6/\alpha$-In_2Se_3 heterostructure under a low electric field E_1, where the polarization state of $CuInP_2S_6$ is pinned by the interfacial state. (d) P–E curve of α-In_2Se_3 corresponding to (c), with the blue line indicating that the P–E curve shifts toward the negative field when the $CuInP_2S_6$ polarization is fixed downward, and the purple line showing a shift toward the positive field when the $CuInP_2S_6$ polarization is fixed upward. (e) Polarization of the $CuInP_2S_6/\alpha$-In_2Se_3 heterostructure under a high electric field E_2, where E_2 exceeds E_{Cr2} and aligns in both polarization directions. (f) The P–E curve of α-In_2Se_3 in the $CuInP_2S_6/\alpha$-In_2Se_3 heterostructure under the strong electric field E_2.

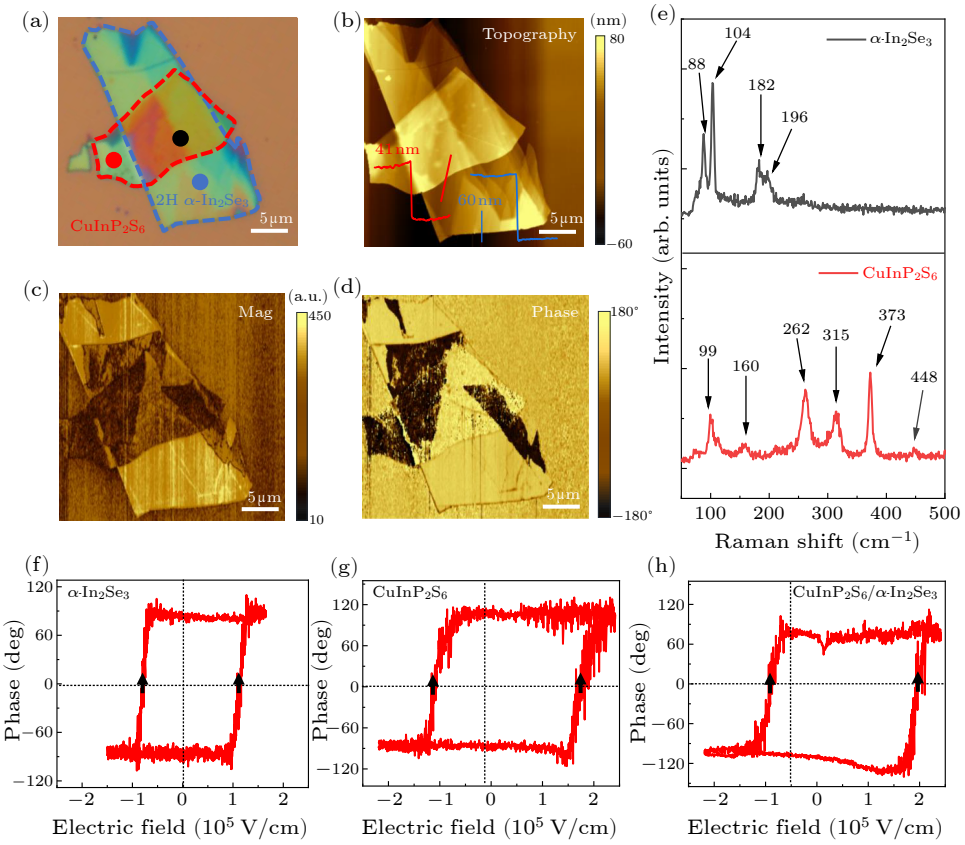

Fig. 2. Characterization of the $CuInP_2S_6/\alpha$-In_2Se_3 heterostructure. (a) Optical image of the $CuInP_2S_6/\alpha$-In_2Se_3 heterostructure. (b) PFM topography image of $CuInP_2S_6/\alpha$-In_2Se_3 with corresponding sample thicknesses of 41 nm ($CuInP_2S_6$, red) and 60 nm (α-In_2Se_3, blue). (c) and (d) Amplitude and phase images corresponding to (b) with the same scale bar. (e) Raman spectra of $CuInP_2S_6$ and α-In_2Se_3. (f)–(h) PFM phase hysteresis of α-In_2Se_3, $CuInP_2S_6$, and $CuInP_2S_6/\alpha$-In_2Se_3 heterostructure with measurement positions indicated in (a) by blue, red, and black indicators, respectively. The intersection of the PFM hysteresis loop with the black straight line at zero phase (indicated by the black arrow) corresponds to the coercive field E_{Cr}.

To validate the above theoretical analysis of the polarization coupling effect, the ferroelectric properties and lattice structure of $CuInP_2S_6/\alpha$-In_2Se_3 heterostructure were characterized using piezoelectric force microscope (PFM) and Raman spectroscopy. As shown in Fig. 2(a), an optical image of $CuInP_2S_6/\alpha$-In_2Se_3 heterostructure on a gold-coated SiO_2/Si substrate is presented, with the red and blue dashed regions indicating $CuInP_2S_6$ and α-In_2Se_3, respectively. Figures 2(b)–2(d) depict the morphology, amplitude, and phase images of the $CuInP_2S_6/\alpha$-In_2Se_3 heterostructure. The images show the thicknesses of $CuInP_2S_6$ and α-In_2Se_3 are 41 nm and 60 nm, respectively, with both materials exhibiting spontaneous polarizations. Notably, the α-In_2Se_3 layer shows clear ferroelectric domains even beneath the thicker $CuInP_2S_6$ layer, revealing distinct polarization directions in both the overlapping and separate regions. In contrast, $CuInP_2S_6$ shows a more uniform polarization, with only a few regions displaying domains with opposite polarization.

Figure 2(e) shows the Raman spectra of exfoliated $CuInP_2S_6$ and α-In_2Se_3 flakes at room temperature, where the peaks at 99, 160, 262, 315, 373, and 448 cm^{-1} correspond to the $CuInP_2S_6$ anion ($P_2S_6^{4-}$), S–P–P, S–P–S, cation (Cu^+, In^{3+}), P–P, and P–S phonon modes.[21] Moreover, α-In_2Se_3 exhibits phonon modes for E, A(LO + TO), A(TO), and A(TO) at 88, 104, 182, and 196 cm^{-1}.[11] Figures 2(f)–2(g) show the phase hysteresis loops measured via PFM for α-In_2Se_3, $CuInP_2S_6$, and the overlapping region of $CuInP_2S_6/\alpha$-In_2Se_3, respectively. The measurement locations are indicated by the red, green, and black solid circles in Fig. 2(a). The results demonstrate that both α-In_2Se_3 and $CuInP_2S_6$ exhibit distinct ferroelectricity with significantly different coercive fields, the coercive field of $CuInP_2S_6$ is notably larger than that of α-In_2Se_3. It is worth noting that the phase hysteresis loops of α-In_2Se_3 and $CuInP_2S_6$ exhibit a shifted hysteresis behavior, which is attributed to the pinning effect of the SiO_2/Si substrate with the evaporated Au on the interface.[21] In the overlapping region of the $CuInP_2S_6/\alpha$-In_2Se_3 heterojunction, the shift effect is more pronounced. This phenomenon supports the hypothesis of the presence of a pinning effect at the ferroelectric interface and is consistent with the positive shift observed in the subsequent I_{ds}–V_{gs} measurements of the graphene/h-BN/$CuInP_2S_6/\alpha$-In_2Se_3/Au FeFET.

To explore the impact of interfacial polarization cou-

pling in 2D ferroelectric heterojunctions on their electrical transport properties, a graphene/h-BN/$CuInP_2S_6$/α-In_2Se_3/Au FeFET is fabricated. As shown in Fig. 3(a), the black, blue, green, and red dashed lines correspond to the top graphene gate electrode, the insulating dielectric h-BN, the ferroelectric gate dielectric $CuInP_2S_6$, and the channel material α-In_2Se_3, respectively (see Fig. S2). When the gate electric field satisfies $E_{Cr1} < |E| < E_{Cr2}$, only the polarization of α-In_2Se_3 is modulated by the gate field, while the polarization of $CuInP_2S_6$ remains unchanged. The schematic representation of the interfacial polarization state under this condition is illustrated in Fig. 3(b). The transfer characteristics of the device under a low gate voltage range is shown in Fig. 3(c), with the source-drain voltage $V_{ds} = 0.1$ V and the gate voltage measurement range from -4 V to $+4$ V, followed by a return measurement (I_{ds}–V_{gs} curves for larger measurement range are shown in Figs. S3–S5). The measurements are conducted at room temperature under a vacuum of 10^{-4} Pa. The I_{ds}–V_{gs} curves exhibit distinct n-type semiconductor behavior and clockwise hysteresis characteristics, with a significant shift in the coercive voltage on both sides of zero gate voltage, as indicated by the red solid arrow in Fig. 3(c). Here, the coercive voltage is defined as V_{gs} corresponding to a significant change in I_{ds}. A clear shift effect is also observed in the I_{ds}–V_{gs} curve, with the shift direction indicating that the polarization direction of $CuInP_2S_6$ is upward and remains unchanged. Meanwhile, the P–E curve of α-In_2Se_3 shows a similar shift, which is consistent with the PFM measurements.

To demonstrate that the observed shift in transfer characteristics of the graphene/h-BN/$CuInP_2S_6$/α-In_2Se_3/Au FeFET at low electric fields is caused by the interface pinning effect of $CuInP_2S_6$ rather than the pinning effect of the SiO_2/Si substrate, a control device is fabricated, namely a graphene/h-BN/α-In_2Se_3/Au FeFET without the $CuInP_2S_6$ gate dielectric, as shown in Fig. 3(d). Figure 3(e) illustrates the interfacial polarization state of α-In_2Se_3 under low electric fields. Under the same conditions, the transfer characteristic curve of α-In_2Se_3 is shown in Fig. 3(f). Within the gate voltage scanning range of ± 4 V, the I_{ds}–V_{gs} transfer characteristic curve also exhibits a similar clockwise hysteresis loop (extended measurements can be found in Fig. S6). However, the I_{ds} change induced by polarization switching in α-In_2Se_3 is less significant compared to that in the $CuInP_2S_6$/α-In_2Se_3 structure, which is related to the enhanced polarization coupling between $CuInP_2S_6$ and α-In_2Se_3.[21] Importantly, the transfer characteristics of α-In_2Se_3 do not show obvious shift effects (the red dashed line indicates the zero gate voltage position). The length of the red solid arrow in Fig. 3(f) is proportional to the magnitude of the coercive voltage in α-In_2Se_3, and it exhibits symmetry around zero voltage. This indicates that the transfer characteristics of the graphene/h-BN/α-In_2Se_3/AuFeFET are not influenced by the pinning effects of the SiO_2/Si substrate, further supporting our previous analysis.

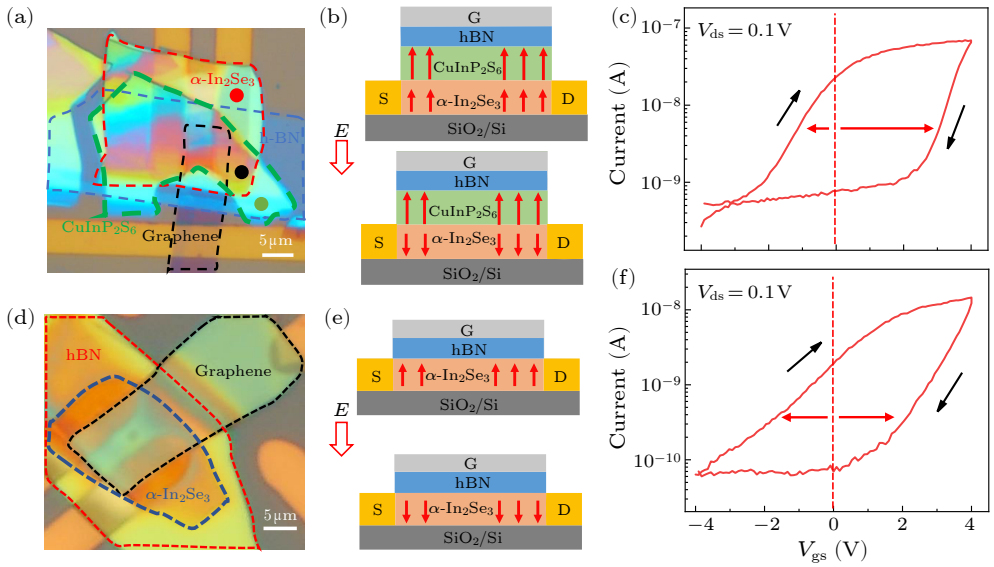

Fig. 3. Electrical transport properties of $CuInP_2S_6$/α-In_2Se_3 and α-In_2Se_3 FeFETs. (a) Optical image of the graphene/h-BN/$CuInP_2S_6$/α-In_2Se_3/Au FeFET, with red, green, blue, and black dashed regions indicating the channel material α-In_2Se_3, gate dielectric $CuInP_2S_6$, gate insulating dielectric h-BN, and top-gate graphene, respectively. (b) Schematic of the interfacial ferroelectric polarization state of graphene/h-BN/$CuInP_2S_6$/α-In_2Se_3/AuFeFET under a low electric field. (c) Transfer curves of graphene/h-BN/$CuInP_2S_6$/α-In_2Se_3/AuFeFET at gate voltages below the coercive field of $CuInP_2S_6$ (E_{Cr2}), with $V_{ds} = 0.1$ V and $V_{gs} = \pm 4$ V, the red dashed line indicates the zero gate voltage. (d) Optical image of the graphene/h-BN/α-In_2Se_3/Au FeFET ferroelectric semiconductor FET. (e) Schematic of the ferroelectric polarization state of graphene/h-BN/α-In_2Se_3/Au FeFET under a low electric field. (f) Transfer curves of the α-In_2Se_3 FeFET at various gate voltages, with $V_{ds} = 0.1$ V and $V_{gs} = \pm 4$ V, showing clockwise hysteresis, the red dashed line indicates the zero gate voltage.

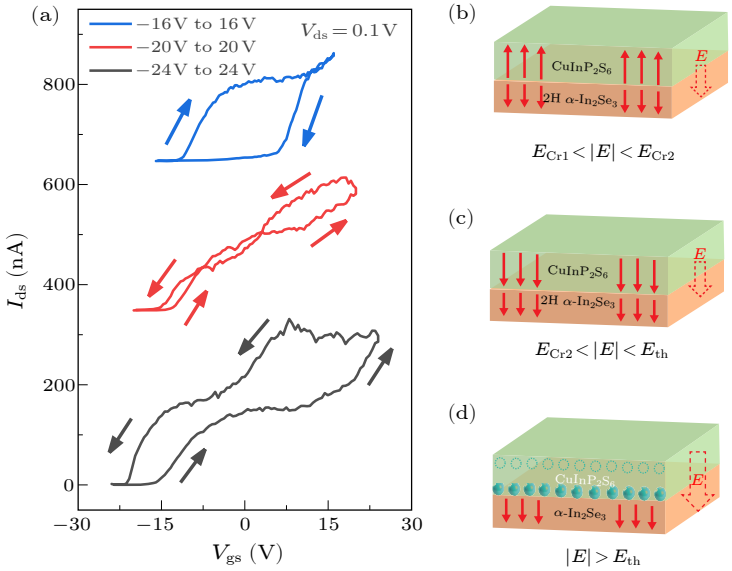

Fig. 4. Gate voltage control of the I–V transfer curve of graphene/h-BN/$CuInP_2S_6$/α-In_2Se_3/Au FeFET. (a) I_{ds}–V_{gs} characteristics of the FeFET at different gate voltage ranges, with $V_{ds} = 0.1$ V. The blue, red, and black I_{ds}–V_{gs} curves represent the transfer characteristics under the conditions of $E_{Cr1} < |E| < E_{Cr2}$, $E_{Cr2} < |E| < E_{th}$, and $|E| > E_{th}$, respectively. (b)–(d) Schematic representations of the interfacial ferroelectric polarization states of $CuInP_2S_6$/α-In_2Se_3 under the conditions of $E_{Cr1} < |E| < E_{Cr2}$, $E_{Cr2} < |E| < E_{th}$, and $|E| > E_{th}$, respectively.

As the measurement range increases, the transfer characteristic curves of the graphene/h-BN/$CuInP_2S_6$/α-In_2Se_3/Au FeFET under different gate voltage ranges exhibit significant differences, as shown in Fig. 4(a). This process can be divided into three distinct scenarios: (1) When the applied gate voltage V_{gs} increases from ±2 V to ±14 V, the width of the α-In_2Se_3transfer characteristic curve increases with the gate voltage and exhibits a reproducible clockwise hysteresis (see Fig. S7). This occurs because the gate electric field, within the range $E_{Cr1} < |E| < E_{Cr2}$, is insufficient to drive polarization switching in $CuInP_2S_6$, thereby modulating only the polarization of α-In_2Se_3, which results in a ferroelectric shift effect. The interface polarization is shown in Fig. 4(b). Additionally, owing to the relatively thick h-BN gate insulator and $CuInP_2S_6$ ferroelectric layer, the external field cannot fully penetrate the α-In_2Se_3 channel layer, leading to partial polarization of α-In_2Se_3. This causes a clockwise hysteresis loop in the transfer characteristics of the device. (2) As the gate voltage increases from ±14 V to ±20 V, the voltage gradually exceeds the coercive field of $CuInP_2S_6$ (E_{Cr2}), but the hysteresis width no longer increases. Instead, it begins to decrease. At this point, the polarization directions of $CuInP_2S_6$ and α-In_2Se_3 remain aligned within this voltage range, as depicted in the interface polarization schematic in Fig. 4(c). This alignment results in the P–E curve of α-In_2Se_3, as shown by the black solid line in Fig. 1(f), allowing for control over the width of the transfer characteristic curve. (3) When the gate voltage continues to increase from ±20 V to ±24 V, the voltage exceeds the threshold field E_{th} of $CuInP_2S_6$, and then Cu ions were driven by the gate field to migrate gradually to the $CuInP_2S_6$/α-In_2Se_3 interface.

To verify that these changes are not directly caused by the external field, we fabricated a comparison device [see Fig. 3(d) and Fig. S6] without the $CuInP_2S_6$ layer. Under gate voltages as high as 34 V, the hysteresis window does not decrease, indicating that the change in the hysteresis direction of the α-In_2Se_3 transfer characteristics is induced by Cu ion migration in $CuInP_2S_6$ above the threshold voltage E_{th}, rather than by the direct penetration of the external electric field into α-In_2Se_3, causing it to transition from partial to complete polarization.[23]

To verify the impact of Cu ion migration in $CuInP_2S_6$ on the electrical transport properties of α-In_2Se_3 under strong electric fields at room temperatures, we perform experiments with different gate electric field scan rates and temperatures. Figure S8 shows the scanning results for gate voltages from −10 V to 10 V at room temperature. When the voltage scan rate is 0.8 V/s, the I_{ds}–V_{gs} hysteresis loop exhibits a clockwise direction, indicating that the polarization direction of $CuInP_2S_6$ is stabilized by interface pinning effect, allowing the electric field to regulate only the polarization of α-In_2Se_3.When the scan rate is reduced to 0.025 V/s, the hysteresis window narrows, suggesting that under strong electric field, the polarization directions of $CuInP_2S_6$ and α-In_2Se_3 become aligned, leading to a decrease in coercive field of α-In_2Se_3. Further reducing the scan rate to 0.008 V/s results in a partially counterclockwise hysteresis loop, attributed to Cu ion migration to the interface, which enhances the regulation of α-In_2Se_3 by $CuInP_2S_6$. To ensure that the gate electric field is sufficiently strong to drive the Cu ions, the scanning voltage range has been extended to ±30 V, as shown in Fig. 5(a). The I_{ds}–V_{gs} curve of α-In_2Se_3 exhibits a counterclockwise hysteresis, indicating that under a strong electric field, even at a fast scanning rate, the Cu ions are effectively driven to migrate to the interface. As the scanning rate decreases, the hysteresis window of the I_{ds}–V_{gs} curve gradually increases.

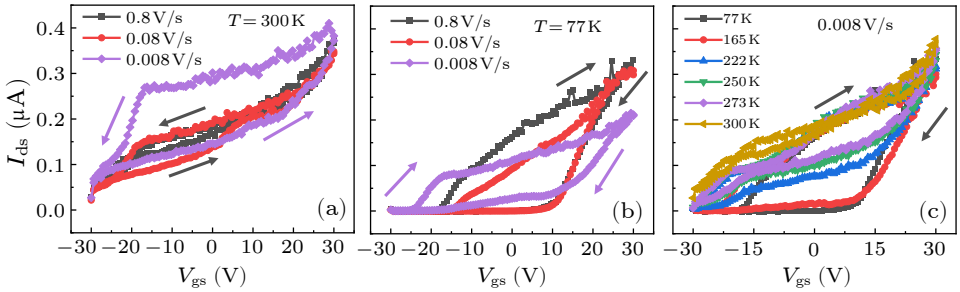

Fig. 5. The effect of scan rate and temperature on Cu ion migration in $CuInP_2S_6$. (a) and (b) The corresponding I_{ds}–V_{gs} transfer characteristics at room temperature (300 K) and low temperature (77 K), with gate voltage scan rates of 0.008 V/s, 0.08 V/s, and 0.8 V/s, respectively. (c) Transfer characteristics of the $CuInP_2S_6$/α-In_2Se_3 heterostructure at different temperatures, with a gate voltage scan rate of 0.008 V/s.

For comparison, the experimental temperature is lowered to 77 K, and the measurements are repeated. The results show that the hysteresis loops of α-In_2Se_3 are maintained in a clockwise direction, with the hysteresis window remaining consistent [see Fig. 5(b)]. This can be attributed to the "freezing" of Cu ions in $CuInP_2S_6$ below 250 K,[24,25] causing the polarization state to remain fixed and unaffected by the electric field. This indicates that at room temperature, Cu ion migration is the main factor responsible for the changes in the transfer characteristics of α-In_2Se_3. To further verify the impact of Cu ion migration on the electrical transport properties of α-In_2Se_3, temperature-dependent experiments are conducted over a wider gate voltage range. Figure 5(c) shows the I_{ds}–V_{gs} curves of α-In_2Se_3 at different temperatures within a ±30 V voltage range, with a gate voltage scanning rate of 0.008 V/s to ensure effective Cu ion migration. The experimental results show that the I_{ds}–V_{gs} hysteresis window of α-In_2Se_3 decreases as the temperature increases, confirming that Cu ion migration under strong electric fields at room temperature is the primary cause of the changes in the transfer characteristics of α-In_2Se_3.

In summary, we successfully fabricate a graphene/h-BN/$CuInP_2S_6$/α-In_2Se_3/Au FeFET and investigate its electrical transport properties under various gate voltages. The experimental results demonstrate that when the gate voltage is below the coercive field of $CuInP_2S_6$, only the polarization of α-In_2Se_3 is modulated, and the transfer characteristics of α-In_2Se_3 exhibit a significant shift due to the interfacial polarization coupling effect. When the gate voltage exceeds the coercive field of $CuInP_2S_6$, the polarization directions of $CuInP_2S_6$ and α-In_2Se_3 are controlled by the external field, modulating the window of the P–E loop curve of α-In_2Se_3 by the different polarization directions of $CuInP_2S_6$. This enables the regulation of the hysteresis window in the transfer characteristics curve of α-In_2Se_3. By applying a gate voltage beyond the threshold field of $CuInP_2S_6$, Cu ions migrate to the $CuInP_2S_6$/α-In_2Se_3 interface. This migration enhances control over the polarization state of α-In_2Se_3 and increases the electron doping concentration, causing the hysteresis loop in the transfer characteristics to gradually shift from clockwise to counterclockwise. Temperature-dependent experiments further confirm that this directional change originates from the migration of Cu ions within $CuInP_2S_6$. This work provides valuable insights for designing multifunctional devices based on ferroelectric ionic material systems.

Acknowledgements. This work is supported by the Chinese Academy of Sciences Project for Young Scientists in Basic Research (Grant No. YSBR-049), the Innovation Program for Quantum Science and Technology (Grant No. 2021ZD0302800), and the Fundamental Research Funds for the Central Universities (Grant No. WK3510000013). This work was partially carried out at the USTC Center for Micro and Nanoscale Research and Fabrication.

References

[1] Li T, Lipatov A, Lu H D, Lee H, Lee J W, Torun E, Wirtz L, Eom C B, Íñiguez J, Sinitskii A, and Gruverman A 2018 *Nat. Commun.* **9** 3344

[2] Bhat T N, Pandey B K, and Krupanidhi S B 2017 *J. Phys. D: Appl. Phys.* **50** 275101

[3] Nishino R, Kozuka Y, Kagawa F, Uchida M, and Kawasaki M 2018 *Appl. Phys. Lett.* **113** 143501

[4] Ye F, Zhang Y, Addiego C, Xu M J, Huyan H X, Ren X B, and Pan X Q 2021 *npj Comput. Mater.* **7** 130

[5] Gao P, Liu H J, Huang Y L, Chu Y H, Ishikawa R, Feng B, Jiang Y, Shibata N, Wang E G, and Ikuhara Y 2016 *Nat. Commun.* **7** 11318

[6] Pei M H, Tian Y, and Zhang J X 2020 *Acta Phys. Sin.* (in Chinese) **69** 217709

[7] Wang X W, Zhu C, Deng Y, Duan R H, Chen J Q, Zeng Q S, Zhou J D, Fu Q D, You L, Liu S, Edgar J H, Yu P, and Liu Z 2021 *Nat. Commun.* **12** 1109

[8] Singh P, Baek S, Yoo H H, Niu J J, Park J H, and Lee S 2022 *ACS Nano* **16** 5418

[9] Si M W, Liao P Y, Qiu G, Duan Y Q, and Ye P D 2018 *ACS Nano* **12** 6700

[10] Liu F C, You L, Seyler K L, Li X B, Yu P, Lin J H, Wang X W, Zhou J D, Wang H, He H Y, Pantelides S T, Zhou W, Sharma P, Xu X D, Ajayan P M, Wang J L, and Liu Z 2016 *Nat. Commun.* **7** 12357

[11] Liaqat A, Yin Y H, Hussain S, Wen W, Wu J X, Guo Y Z, Dang C H, Ho C H, Liu Z, and Yu P 2022 *Nanotechnology* **33** 125703

[12] Li W Y, Guo Y M, Luo Z P, Wu S H, Han B, Hu W J, You L, Watanabe K, Taniguchi T, Alava T, Chen J Z, Gao P, Li X Y, Wei Z M, Wang L W, Liu Y Y, Zhao C X, Zhan X P, Han Z H, and Wang H W 2023 *Adv. Mater.* **35** 2208266

[13] Huang W H, Wang F, Yin L, Cheng R Q, Wang Z X, Sendeku M G, Wang J J, Li N N, Yao Y Y, and He J 2020 *Adv. Mater.* **32** 1908040

[14] Xue F, He X, Liu W H, Periyanagounder D, Zhang C H, Chen M G, Lin C H, Luo L Q, Yengel E, Tung V, Anthopoulos T D, Li L J, He J H, and Zhang X X 2020 *Adv. Funct. Mater.* **30** 2004206
[15] Wan S Y, Li Y, Li W, Mao X Y, Wang C, Chen C, Dong J Y, Nie A M, Xiang J Y, Liu Z Y, Zhu W G, and Zeng H L 2019 *Adv. Funct. Mater.* **29** 1808606
[16] Liu K Q, Zhang T, Dang B J, Bao L, Xu L Y, Cheng C D, Yang Z, Huang R, and Yang Y C 2022 *Nat. Electron.* **5** 761
[17] Li Y, Chen C, Li W, Mao X Y, Liu H, Xiang J Y, Nie A M, Liu Z Y, Zhu W G, and Zeng H L 2020 *Adv. Elect. Mater.* **6** 2000061
[18] Bao Y, Song P, Liu Y P, Chen Z H, Zhu M L, Abdelwahab I, Su J, Fu W, Chi X, Yu W, Liu W, Zhao X X, Xu Q H, Yang M, and Loh K P 2019 *Nano Lett.* **19** 5109
[19] Higashitarumizu N, Kawamoto H, Lee C J, Lin B H, Chu F H, Yonemori I, Nishimura T, Wakabayashi K, Chang W H, and Nagashio K 2020 *Nat. Commun.* **11** 2428
[20] Wang W J, Meng Y, Wang W, Zhang Y X, Li B W, Yan Y, Gao B X, and Ho J C 2023 *Mater. Today Electron.* **6** 100080
[21] Baek S, Yoo H H, Ju J H, Sriboriboon P, Singh P, Niu J J, Park J H, Shin C, Kim Y, and Lee S 2022 *Adv. Sci.* **9** 2200566
[22] Zhang D W, Luo Z D, Yao Y, Schoenherr P, Sha C H, Pan Y, Sharma P, Alexe M, and Seidel J 2021 *Nano Lett.* **21** 995
[23] Si M W, Saha A K, Gao S J, Qiu G, Qin J K, Duan Y Q, Jian J, Niu C, Wang H Y, Wu W Z, Gupta S K, and Ye P D 2019 *Nat. Electron.* **2** 580
[24] Zhong Z P, Wu S Q, Li X, Wang Z Q, Yang Q Y, Huang B C, Chen Y, Wang X D, Lin T, Shen H, Meng X J, Wang M, Shi W, Wang J L, Chu J H, and Huang H 2023 *ACS Nano* **17** 12563
[25] Zhou J C, Chen A Z, Zhang Y S, Pu D, Qiao B S, Hu J Y, Li H X, Zhong S, Zhao R, Xue F, Xu Y, Loh K P, Wang H, and Yu B 2023 *Adv. Mater.* **35** 2302419